NJC

ROYAL SOCIETY OF CHEMISTRY

PAPER

View Article Online
View Journal | View Issue

Cite this: *New J. Chem.*, 2025, 49, 18623

Cu-based coordination polymer@GO for supercapacitor and solid-state proton conduction applications

Richa Rajak, Kushagra Sinha, Sweety Gupta and Amit Paul *

Redox-active linkers containing conjugated coordination polymers (CPs) are promising materials for energy storage/conversion devices owing to their superior multi-electron redox properties compared to conventional CPs. Further incorporation of conducting materials into CPs can be an effective approach towards upgrading their electrochemical performance. In this work, a redox-active *N*,*N*-di(4-pyridyl)-1,4,5,8-naphthalenetetracarboxydiimide (DPNDI) linker self-assembled with the Cu(II) ion has been synthesized, introducing a 3D supramolecular structure of $[Cu(DPNDI)(NO_3)_2(CH_3CN)]_n$, (Cu-CP). Benefitting from the advantage of graphite oxide (GO) and redox-active Cu-CP, herein, we report the fabrication of a Cu-CP@GO composite through a solvothermal approach. Cu-CP@GO exhibited an excellent specific capacitance of 178 F g^{-1} at 0.6 A g^{-1} in a three-electrode configuration, significantly higher than that of pristine Cu-CP. Furthermore, a two-electrode symmetric device made of Cu-CP@GO exhibited a high specific capacitance of 93 F g^{-1} at 0.5 A g^{-1} and a cycling stability of 96% after 5000 cycles (50 h), in spite of *in situ* generation of radical anions during redox transitions. This was attributed to excellent charge delocalization in the π-network of the NDI ligand and GO. Additionally, Cu-CP@GO demonstrated a high solid-state proton conductivity of 1.4 × 10^{-3} S cm^{-1} at 95 °C and 95% RH, along with a low activation barrier of 0.33 eV, revealing proton migration by the Grotthuss mechanism. This exceptional supercapacitor performance and solid-state proton conductivity of Cu-CP@GO are attributed to the enhanced electrical conductivity resulting from the synergistic effect of CP and GO.

Received 30th July 2025,
Accepted 30th September 2025

DOI: 10.1039/d5nj03093e

rsc.li/njc

Introduction

In recent decades, increasing energy demand has compelled scientists to develop efficient energy storage devices with high energy and power densities. Clean energy storage technologies are the key components for storing energy from intermittent renewable sources like wind turbines and solar photovoltaics.[1,2] Thus, energy storage systems, for instance supercapacitors and batteries, have the ability to lessen this intermittency issue by storing the produced energy for later use when needed.[3] Supercapacitors have emerged with enticing energy properties owing to their high charge–discharge times and excellent power density.[1–3] They are classified as hybrids, pseudocapacitors, and EDLCs, which highlights the differences in their material requirements and mechanisms. The EDLC mechanism depends on electrostatic ion adsorption at the electrode–electrolyte interface. On the other hand, pseudocapacitors increase capacitance by using surface or near-surface redox processes.[4] They have important applications in rapid energy storage and electric vehicles. Commercial supercapacitors commonly use porous carbon due to their decent electrical conductivity, large surface area for charge storage, and high cycling stability.[5] However, it is difficult to control the nanostructure of porous carbon, and there are limited approaches for incorporating new functionality to meet the high capacitance requirements.[6–9] Recently, the research scenario has shifted towards developing hybrid organic–inorganic solids, promising materials for various sustainable energy applications.[10–12] The expansion of crystalline coordination polymers (CPs) by the molecular self-assembly of organic linkers with inorganic metal centers has revolutionized access to modular solid-state materials.[13,14] The deliberate selection of tunable building block molecules has offered a wide range of CP-based solid-state networks having applications in sensing, catalysis, gas storage, energy storage, energy conversion, *etc.*[15–19] However, the fragile structure and low intrinsic electrical conductivity of the majority of MOFs/CPs have limited their application in electrochemical and electronic devices.[19] Therefore, redox-active and electrochemically conductive MOFs/CPs

Department of Chemistry, Indian Institute of Science Education and Research (IISER) Bhopal, Bhopal-bypass Road, Bhauri, Bhopal, MP, India 462066.
E-mail: apaul@iiserb.ac.in

have emerged and been developed for electrochemical applications such as supercapacitors, batteries, and electrocatalysis.[20–22] Redox-active linkers often contain π-electron systems, facilitating charge delocalization throughout the frameworks.[23,24] In this regard, naphthalene diimides (NDI) have attracted considerable interest owing to their high electron affinity, superior charge mobility, reversible redox characteristics, good solubility, remarkable self-assembly, and oxidative stability.[20,25–27] Pseudocapacitive materials with redox-active centers show high capacitance but low cycling stability due to their smaller surface area and lack of uniform porosity.[17,24,28] Therefore, there is a need to develop electrode materials that combine conducting materials and redox-active centers that synergistically enhance the overall performance of composite materials by improving their conductivity. Recently, graphite oxide (GO) has been proven to be a potential material for electrochemical applications due to its high electrical conductivity and mechanical robustness.[29–31] Composite materials of CPs and GO may not only enhance the conductivity but also facilitate electron transfer for better supercapacitor performance.[32–34]

Besides, CP/GO composites emerged as functional materials for solid-state proton conduction, which can be utilized for proton exchange membrane fuel cells (PEMFCs) and other sensing applications.[32,35,36] The composites integrate the benefits of both CPs and GO. Traditionally, Nafion has been employed as a proton-conducting material in these systems, but its high synthesis cost, perfluorinated nature, and high-temperature operational limitation hinder its widespread utilization.[37] In general, there are two primary approaches for the rational design of CPs for achieving enhanced proton conductivity.[38] The first approach is the functionalization of ligands based on intrinsic proton sources. There are several reports based on CPs with intrinsic proton sources such as uncoordinated $-SO_3H$, $-PO_3H_2$, NO_3^-, and $-COOH$ groups oriented toward the pore channels, as well as the presence of protic species such as H_3O^+, $Me_2NH_2^+$, NH_4^+, *etc.* which showed enhanced proton conduction.[39–41] The second approach involves the integration of CPs with other nanomaterials, including GO, which has been demonstrated as an effective way to improve proton conductivity of the resultant composite.[42–44] Based on the principles of rational design outlined previously, the present work involves the synthesis of an innovative CP-based composite material, with the aim of utilizing it in the development of high-performance composite proton exchange membranes. However, less effort has been made to construct CPs with redox-active center-based materials that are deliberately used for energy storage and conversion applications.

Herein, we report the synthesis of $[Cu(DPNDI)(NO_3)_2(CH_3CN)]_n$ (Cu-CP), strategically introducing the DPNDI linker comprising a redox-active core (NDI) and Cu(II) metal nodes to develop a 3D supramolecular network. The DPNDI linker was chosen to encapsulate metal nodes and form unique frameworks with interesting properties.[25,45] Besides, the NDI redox-active core demonstrates two consecutive one-electron redox reactions and π-conjugation that maximize charge transfer mobility and electrical conductivity.[45] Cu-CP exhibited two successive reductions, generating very stable radical anion and dianion species (Fig. S1). Furthermore, a composite material Cu-CP@GO was prepared using a simple solvothermal methodology. Even with a relatively low surface area, Cu-CP@GO exhibited excellent electrical conductivity, which led to its exceptional electrochemical application potential. The supercapacitor performances of both materials were evaluated under similar conditions, and Cu-CP@GO exhibited a superior performance. Redox-active Cu-CP contributed pseudocapacitive behavior, while GO provided mechanical stability, and thus prevented aggregation and provided a conducting pathway that synergistically enhanced the overall electrochemical performance of the composite material by improving its conductivity. Additionally, the nitrate anions in Cu(II) ions helped in increasing the acidity of the metal center, which facilitated the immobilization of protons within hydrogen-bonded matrices and contributed towards improved proton conductivity. Additionally, the hydrophilic groups present in GO, such as hydroxyl, carboxyl, epoxy, *etc.*, helped in creating multiple conduction pathways for proton conduction.

Experimental section

Materials

Copper(II) nitrate trihydrate ($Cu(NO_3)_2{\cdot}3H_2O$), 4-amino pyridine, 1,4,5,8 naphthalenetetracarboxylic dianhydride, *N*-methyl-2-pyrrolidone (NMP), acetonitrile, dimethylformamide (DMF), acetylene black, graphite oxide, diethyl formamide (DEF), sodium dihydrogen phosphate (NaH_2PO_4), polyvinylidene fluoride (PVDF), dimethyl acetamide (DMA), disodium hydrogen phosphate (Na_2HPO_4), ethanol, and acetone were purchased from Sigma Aldrich and BLD Pharma and used without purification. For electrochemical studies, platinum (Pt) foil, a platinum (Pt) wire, and a saturated calomel electrode (SCE) were purchased from Sinsil International, India (supplied from CH Instrument, TX, USA). A bipotentiostat (model CHI 760D) and BioLogic SP300 and SP240 were used for electrochemical characterization. Steel 47 electrodes containing two probe cells for proton conductivity measurements were purchased from BioLogic, India.

Synthesis of Cu-CP

Initially, the DPNDI linker was prepared *via* a one-step approach following a reported method.[46] In a round-bottom flask, 1,4,5,8 naphthalenetetracarboxylic dianhydride (200 mg, 0.7 mmol) and 4-aminopyridine (154 mg, 1.4 mmol) were mixed with 30 mL diethyl formamide (DEF) solvent and refluxed at 130 °C for 48 h under an inert atmosphere. After completion, the mixture was left to cool at room temperature and subsequently stored in a refrigerator for better precipitation. After two days, it was then filtered with distilled water and ethanol solvent and dried in an oven for 24 h at 80 °C. Thereafter, DPNDI was utilized as a precursor in subsequent processes. Cu-CP was synthesized by a slow diffusion technique at room temperature.[47] In this process, DPNDI (8.4 mg, 0.02 mmol) and $Cu(NO_3)_2{\cdot}3H_2O$ (10 mg, 0.04 mmol) were dissolved separately in

10 mL of DMA and 10 mL acetonitrile, respectively, and a buffer solution was made using acetonitrile and dimethyl formamide in a 1 : 1 ratio. Subsequently, 2 mL of metal salt solution was layered above 2 mL of DPNDI organic linker solution in a narrow glass test tube using 1 mL of buffer solution. The tube was closed with a parafilm and placed undisturbed at room temperature. After a week, blue-colored crystals were obtained by the diffusion of the layers. The crystals were collected and dried in the air. Then, the bulk powder compound of Cu-CP was synthesized by directly mixing the DPNDI solution into the metal solution and stirring overnight at room temperature. The mixture was then filtered and air-dried. Yield 56%. FT-IR (cm^{-1}): 1669(s), 1582(m), 1356(s), 1251(w), 771(m), 652(m).

Synthesis of Cu-CP@GO

Graphite oxide (GO) was prepared using Hummers' method by following a previously reported methodology of our group.[30,48] By using Cu-CP and GO as precursors, Cu-CP@GO was synthesized *via* a solvothermal method. In a round bottom flask, 100 mg of Cu-CP and 100 mg of GO (1 : 1 weight ratio) were taken in 30 mL DMF and sonicated for 2 h for better homogeneity and then poured into a Teflon-linked autoclave. The autoclave was tightly sealed and kept in an oven for 24 h at 100 °C. It was thereafter allowed to cool to room temperature inside an oven for slow diffusion. Similarly, two more Cu-CP@GO composites were prepared by taking different ratios of Cu-CP and GO (3 : 1 and 1 : 3 weight ratio). Furthermore, all materials were filtered and dried in an oven at 80 °C overnight before being used.

Electrode fabrication for supercapacitor studies

For electrode fabrication, the active material was coated on the platinum (Pt) foil. First, Pt foil was sonicated in acetone for approximately 30 min to ensure cleaning, followed by air drying. Pt electrodes were prepared by coating them with an active material slurry of 6 mg of Cu-CP@GO or Cu-CP, 2 mg of acetylene black (AC), and 1 mg of PVDF dissolved in 1 mL of NMP. The mixture was blended for 6 h to ensure homogeneity. A 100 μL aliquot of this mixture was then drop-cast on 1 cm^2 Pt foil electrodes, dried in an oven at 100 °C for around 16 h, and later used as working electrodes for electrochemical studies. The active mass of materials is 0.8 mg cm^{-2} on the working electrodes. For a two-electrode symmetric device, 100 μL of material was drop-cast on Pt-foil, and two electrodes were inserted in a Swagelok cell and separated by Whatman filter paper soaked in PVA/H_2SO_4.

Proton conductivity measurement

Proton conductivity measurements were performed using a two-probe measurement. 120 mg of the sample was pressed in a hydraulic press with 5 tons of pressure to obtain a pellet of 0.4–0.5 mm thickness and a diameter of 13 mm. Prior to each experiment, the samples were allowed to reach equilibrium for nearly 2 h for temperature-dependent studies and 3 h for humidity-dependent experiments. The resistance corresponding to the proton transfer was determined by an EIS equivalent circuit that fitted the semicircle of the Nyquist plot.

Results and discussion

Preparation of Cu-CP@GO is illustrated in Scheme 1. GO was prepared using Hummers' method with minor modifications following our group's previous report.[30,48] Initially, the light-blue colored crystals of Cu-CP were obtained by a slow diffusion approach using $Cu(NO_3)_2{\cdot}4H_2O$ and the *N*,*N*-di(4-pyridyl)-1,4,5,8-naphthalenetetracarboxydiimide (DPNDI) ligand in a 1 : 2 ratio at room temperature. The structural and coordination

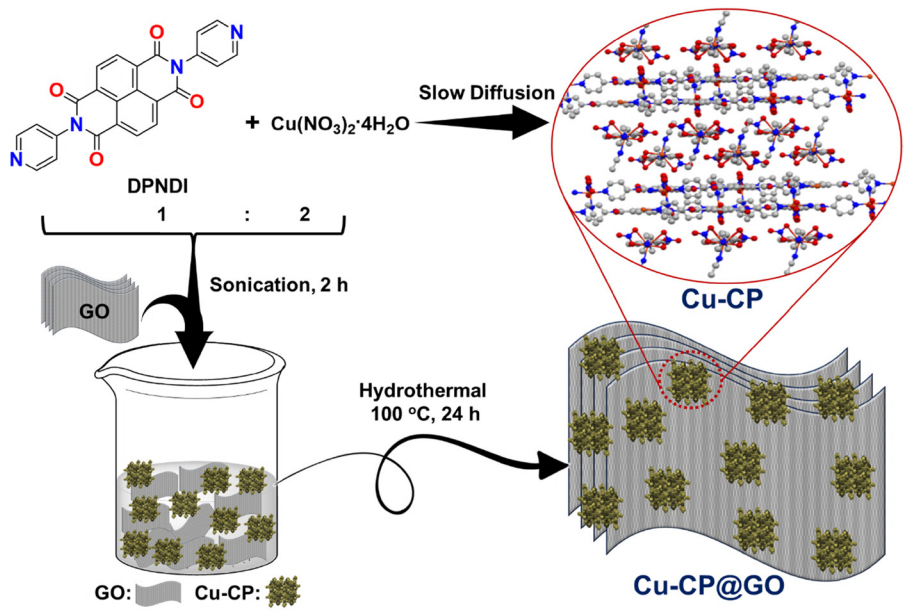

Scheme 1 Schematic representation of the synthesis of Cu-CP and Cu-CP@GO.

sphere of Cu-CP was characterized by single-crystal X-ray analysis. Furthermore, to construct Cu-CP@GO, Cu-CP was dispersed in GO by a hydrothermal approach at 100 °C for 24 h. The Cu-CP presumably formed noncovalent interactions with GO. Cu-CP was presumably immobilized on the surface and edges of GO sheets through the hydrogen bonding with the oxygen functionalities present in GO and through the π···π stacking interactions. The physicochemical properties of the as-synthesized Cu-CP and Cu-CP@GO compounds have been characterized by PXRD, TGA, FT-IR, SEM, TEM, BET and XPS spectroscopic techniques. Furthermore, Cu-CP@GO exhibited superior electrochemical behavior towards supercapacitor and proton conduction applications (*vide infra*).

Characterization

The PXRD analysis of both materials was performed to study the bulk formation of Cu-CP and Cu-CP@GO (Fig. 1a). All the major peaks of the as-synthesized Cu-CP spectrum matched well with the simulated ones obtained from the SCXRD, confirming the bulk purity of polycrystalline Cu-CP. A minor shift in the PXRD spectrum was observed, which could be due to sample preparation, instrumental error, or solvent removal. GO showed characteristic peaks at 10.3° and 42.3° (Fig. S2), matching well with previously reported works.[30,48] The PXRD spectrum of Cu-CP@GO showed the characteristic peaks of Cu-CP and GO. Two broad diffraction peaks appeared at the 2θ values of ∼11° and ∼43°, which can be assigned to (002) and (100) planes, respectively.[49] Additionally, one broad diffraction peak appeared at ∼24°, suggesting partial restoration of the graphitic structure during thermal treatment.[50] Furthermore, the PXRD spectra of Cu-CP@GO having different ratios of Cu-CP and GO were recorded, which show characteristic peaks of Cu-CO and GO (Fig. S3). It was observed that with increasing amount of GO, significant suppression of Cu-CP crystalline peaks was observed. A decrease in the intensity of Cu-CP peaks in Cu-CP@GO can be attributed to its effective binding with GO, indicating the proper growth of Cu-CP on GO sheets without deforming the structure of Cu-CP. Additionally, thermogravimetric analysis (TGA) was performed to check the thermal stability of Cu-CP and Cu-CP@GO (Fig. 1b). TGA studies revealed that Cu-CP and Cu-CP@GO were thermally stable up to 185 °C and 251 °C, respectively, demonstrating enhanced thermal stability of Cu-CP@GO compared to Cu-CP. Both materials exhibited stepwise weight loss curves, and a rapid weight loss occurred at higher temperature (360 °C), corresponding to the breakdown of organic moieties. The enhanced thermal stability of Cu-CP@GO can be ascribed to the synergistic interaction between Cu-CP and GO.

The FESEM and TEM images of Cu-CP and Cu-CP@GO are depicted in Fig. 2 and Fig. S4. The SEM images of Cu-CP showed a block-shaped morphology with sizes varying ∼0.2–0.5 μm (Fig. S4a). The TEM images confirmed a block-shaped morphology, which is in good agreement with SEM images (Fig. S4b). Furthermore, the SAED pattern revealed intense diffraction spots, demonstrating the good crystalline nature of the prepared Cu-CP (Fig. S4c). Fig. S4d illustrates the selected area of the TEM image for the EDX elemental analysis and mapping, demonstrating the uniform distribution of all elements and validating the presence of Cu, C, O, and N elements (Fig. S4e–i). The SEM images of Cu-CP@GO manifest the proper growth of Cu-CP on the surface and edges of the GO sheets, which further confirmed the block-shaped morphology of Cu-CP with an average size of 0.5 μm (Fig. 2a and b). The strong electrostatic interactions were liable for the Cu-CP growth on GO Sheets that were negatively charged owing to the occurrence of oxygen functional moieties and Cu(II) cations of Cu-CP. EDX analysis elucidates the presence of Cu, C, O and N atoms (Fig. 2c), and elemental mapping reveals the uniform distribution throughout the examined surface (Fig. 2d–g). The TEM images validate that the dispersed Cu-CP block-shaped particles were embedded in the GO sheets maintaining their morphology (Fig. 2h and i). The SAED pattern shows concentric rings with diffraction spots, revealing the crystalline nature of Cu-CP@GO (Fig. 2j). Hence, it can be inferred that the morphology of Cu-CP in Cu-CP@GO remained the same even after the formation of the composite material.

Surface N_2 adsorption/desorption isotherms at 77 K were obtained to determine the BET surface area and BJH pore size of Cu-CP and Cu-CP@GO, as shown in Fig. S5a. Isotherm profiles of Cu-CP and Cu-CP@GO exhibited a characteristic

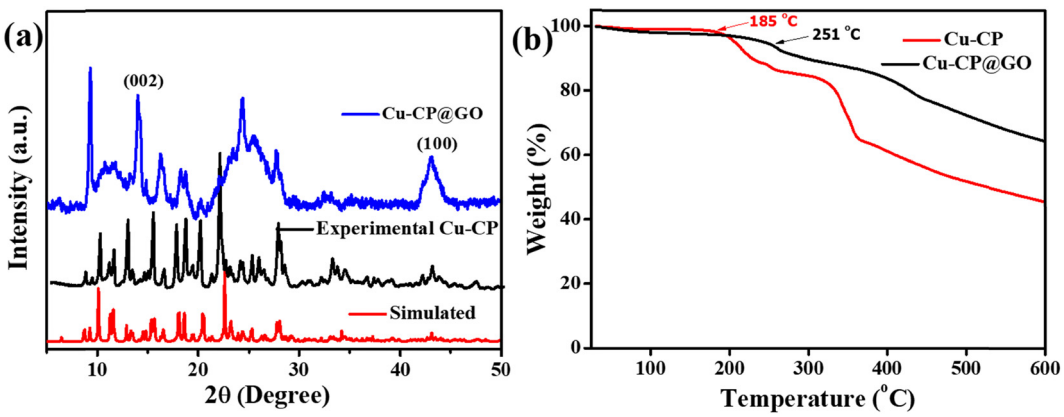

Fig. 1 (a) PXRD spectra of simulated (red), experimental Cu-CP (black) and Cu-CP@GO (blue), (b) TGA profiles of Cu-CP and Cu-CP@GO.

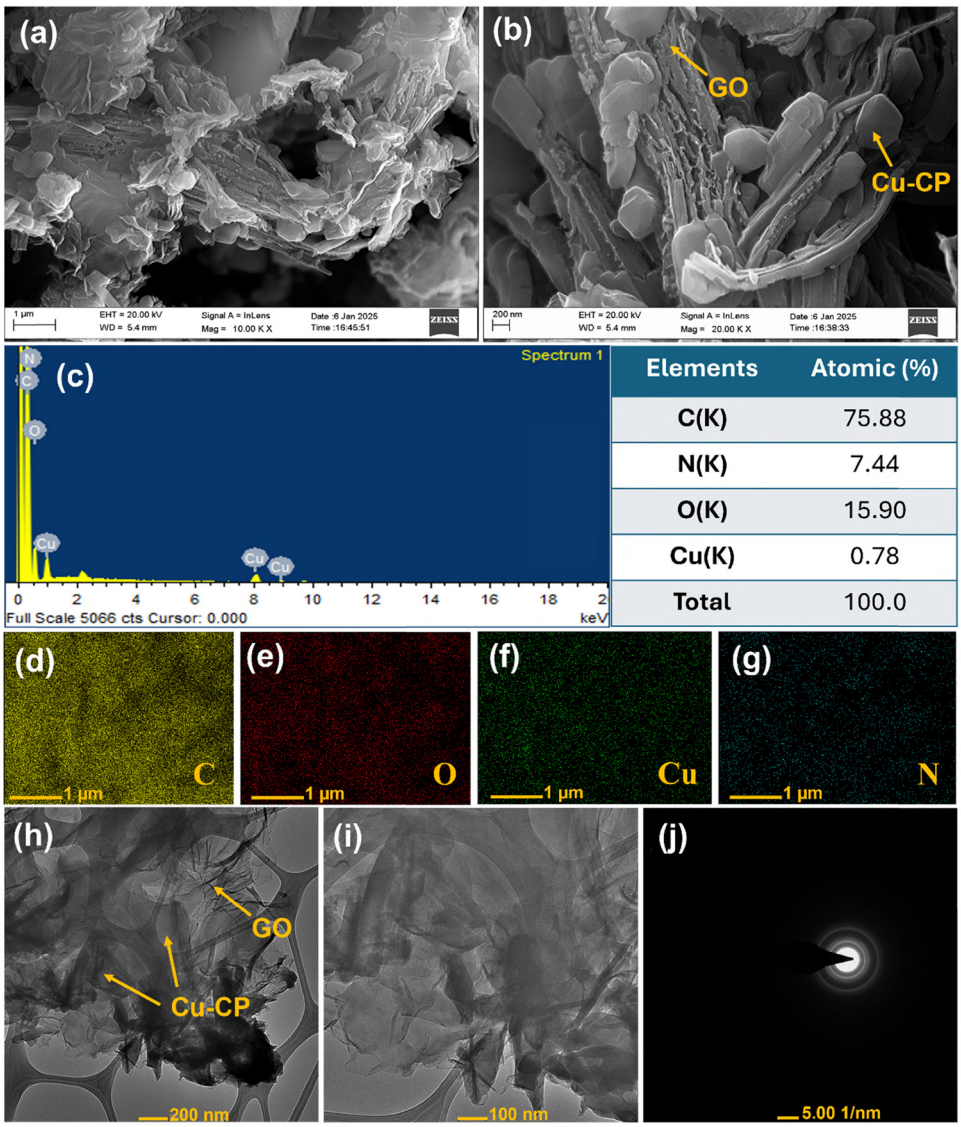

Fig. 2 (a) and (b) SEM images of Cu-CP@GO at different magnifications, (c) EDX analysis results, (d)–(g) elemental mapping, (h) and (i) TEM images of Cu-CP@GO at different magnifications and (j) SAED patterns.

type IV adsorption/desorption isotherm featuring a H3 type hysteresis, indicating mesoporous nature as per IUPAC classification.[51] The BET specific surface area of Cu-CP was low (7 m^2 g^{-1}), while that of Cu-CP@GO was 14 m^2 g^{-1}. The corresponding pore distribution was determined using the Barrett–Joyner–Halenda (BJH) method as listed in Table S1 (Fig. S5b–d). The FT-IR spectrum of Cu-CP shows the characteristic peaks for C═O, C═C, C–N, C–O, Cu–N and Cu–O at 1669, 1582, 1251, 1356, 771 and 652 cm^{-1}, respectively (Fig. S6). The FT-IR spectrum of Cu-CP@GO reveals a strong broad peak at 3302 cm^{-1} attributed to –OH and –COOH functionalities (Fig. S7a). The other essential bands in the frequencies can be attributed to C═O, C═C, C–O, C–N, Cu–N, and Cu–O at 1675, 1573, 1346, 1246, 764, and 624 cm^{-1}, respectively (Fig. S7a).[30,52] Cu-CP@GO was further investigated using XPS to determine its surface composition, oxidation state of Cu and deconvoluted spectra to understand the chemical bonding. Fig. S7b illustrates a survey scan, manifesting the presence of C, O, N, and Cu elements. The Cu 2p spectrum demonstrates two peaks of Cu $2p_{3/2}$ (934.3 eV) and Cu $2p_{1/2}$ (954.3 eV) associated with strong satellite peaks of Cu $2p_{3/2}$ (~939.7–943 eV) and Cu $2p_{1/2}$ (~962.6 eV), which confirm the divalent oxidation state of Cu (Fig. S7c).[52] Subsequently, the C 1s scan shows four significant peaks at 288.8, 286.8, 285.6, and 284.6 eV ascribed to C═O, C–O, C–C/C–N, and C═C, respectively (Fig. S7d).[30] The N 1s scan reveals three distinct peaks of pyridinic-N, N–(C═O), and graphitic-N at 399.5, 400.7 and 401.3 eV, respectively (Fig. S7e).[53] The O 1s scan exhibits three peaks at 532.9 (C–O), 532.3 (–O–C═O), 531.5 (C═O) and 531.2 eV (O–H), revealing the oxygen functionalities in Cu-CP@GO (Fig. S7f).[54] The above evidence confirmed the formation of Cu-CP@GO composite that has the potential to show excellent electrochemical performance (*vide infra*).

The electrical conductivity was measured using the two-probe method and was found to be 8.1 × 10^{-2} S cm^{-1} for

Cu-CP (Fig. S8). In contrast, the composite Cu-CP@GO exhibited a higher conductivity of 1.14×10^{-1} S cm^{-1} (Fig. S8). This was attributed to the incorporation of GO into Cu-CP, which significantly enhanced the electrical conductivity due to π electron delocalization and facilitated electron movement in the composite.

Structural description of Cu-CP

Cu-CP crystallized in the monoclinic crystal system with a $P2_1/c$ space group. The asymmetric unit comprises one Cu(II) ion, one DPNDI ligand, and two coordinated nitrate anions, along with one coordinated acetonitrile molecule (Fig. S9). As depicted in Fig. 3a, each Cu(II) ion was coordinated to two nitrogen atoms of the DPNDI ligand and one nitrogen atom of the coordinated acetonitrile molecule and four oxygen atoms of the coordinated nitrate anions. Each Cu(II) ion was in the O_4N_3 coordination sphere and formed a distorted pentagonal bipyramidal geometry, and the charge of the Cu(II) ion was balanced by the presence of two coordinated nitrate anions (Fig. 3b). The measured bond length of Cu–O was in the range of 2.015(7) Å to 2.017(6) Å, while the Cu–N distance ranged from 1.980(6) Å to 2.241(11) Å. Crystal refinement data and other significant bond lengths and bond angle tables are summarized in Tables S2–S4. Each DPNDI ligand was coordinated to Cu(II) ions and generated a one-dimensional (1D) chain view along the *a*-axis (Fig. 3c). Furthermore, these resulting 1D layers were interconnected to each other through noncovalent interactions such as H-bonding, C–H···π, and π···π stacking interactions and constructed a 3D supramolecular framework along the *b*-axis where the distance between two consecutive 1D layers was 3.889 Å (Fig. 3d). Additionally, the redox-active DPNDI ligand demonstrated two consecutive one-electron redox reactions that resulted from the reduction of NDI core motifs to the radical anion $NDI^{\bullet -}$ and dianion NDI^{2-} species (Scheme 2 and Fig. S1).[45] The redox-active behavior of Cu-CP helped to achieve excellent electrochemical performance (*vide infra*).

Electrochemical studies of Cu-CP and Cu-CP@GO

The redox-active nature of the DPNDI linker inspired us to investigate the supercapacitor behavior of both materials, wherein Cu-CP@GO consisted of DPNDI as redox-active sites and GO as a conductive material, which holds substantial potential for renewable energy applications. Therefore, cyclic

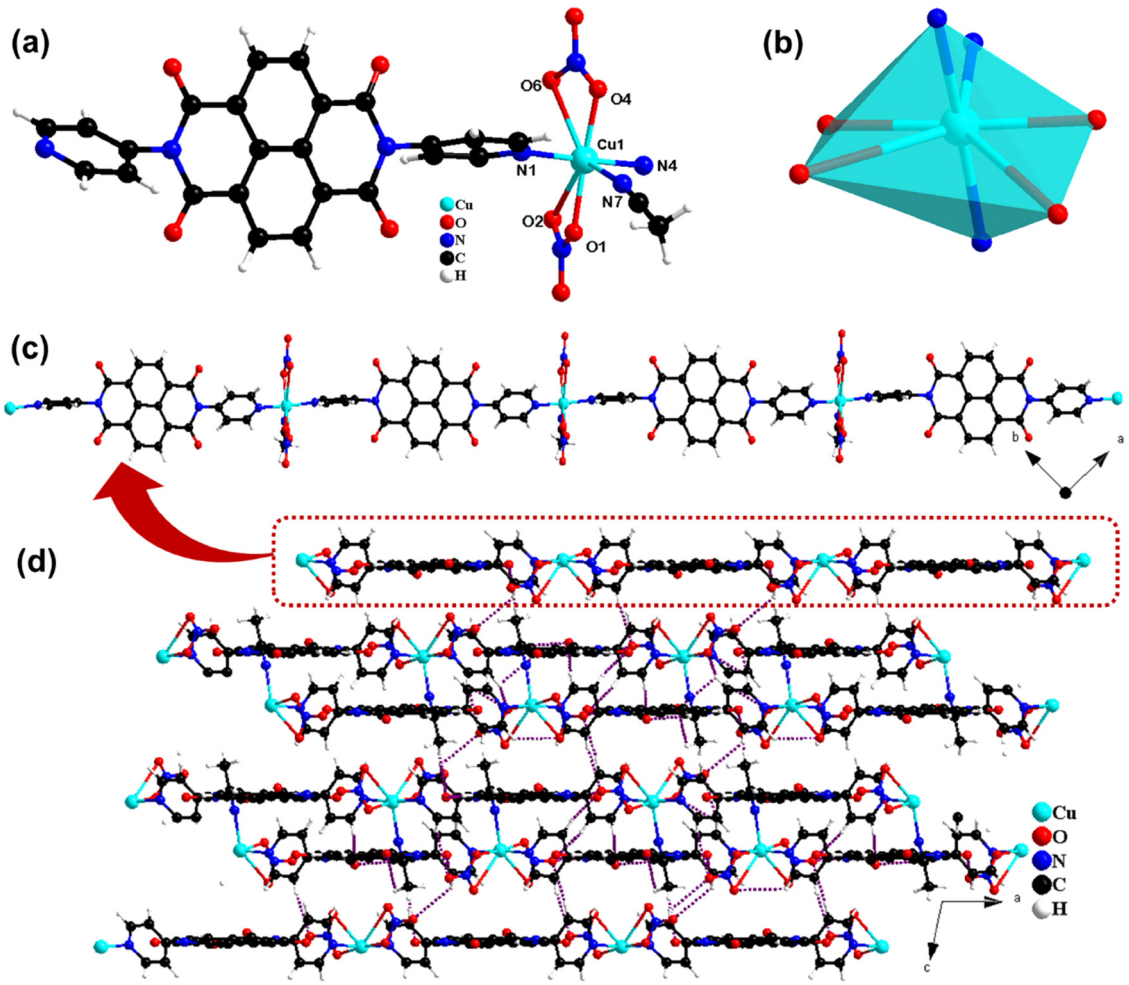

Fig. 3 (a) Molecular unit of Cu-CP, (b) distorted pentagonal bipyramidal geometry around the Cu(II) metal ion, (c) 1D chain along the *c*-axis, and (d) 3D supramolecular network along the *b*-axis.

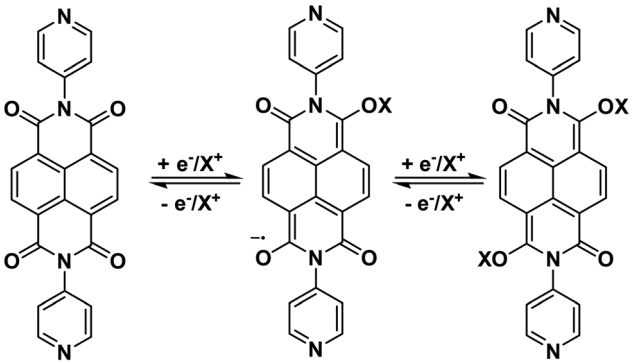

Scheme 2 Redox reaction of DPNDI in Cu-CP@GO, showing the radical anion and dianion formation (X^+ is the electrolyte cation).

voltammetry studies of Cu-CP and Cu-CP@GO were performed in a three-electrode setup using a 1 cm^2 Pt foil-coated material (working electrode), SCE (reference electrode), and a Pt wire (counter electrode). The potential range of (−)0.7 to 0.4 V (*vs.* SCE) was maintained using phosphate buffer (pH 7.5) as an electrolyte to ensure the structural integrity of the material during electrochemical tests. The CV profiles of Cu-CP, GO, and Cu-CP@GO composites formed with varying ratios of the participating constituents, *i.e.*, Cu-CP and GO, were first recorded in order to obtain mechanistic insights and examine the effects of the ratio of the participating constituents on the electrochemical properties. The CVs at a scan rate of 50 mV s^{-1} are shown in Fig. S10, indicating that the introduction of GO improved charge propagation and enhanced current response. Cu-CP@GO composites had a higher current response compared to pristine Cu-CP and GO. It was observed that the area under the CV curve of composites increased up to a 1 : 1 ratio of Cu-CP and GO, and thereafter declined. This indicated that perfect synergy occurred with an equal ratio of Cu-CP and GO. Hence, we opted to use Cu-CP@GO prepared with a 1 : 1 ratio for further studies. Moreover, comparative CVs of GO and Cu-CP@GO evidenced that the area under the CV curve of Cu-CP@GO was significantly higher than that of GO (Fig. S10), exhibiting a specific capacitance value 5.6 times higher than that of GO.

The CV experiments were carried out at scan rates ranging from 2 to 50 mV s^{-1}, which provided pertinent insights into the charge/discharge characteristics. Fig. 4a shows the CVs of Cu-CP and Cu-CP@GO at 50 mV s^{-1}, and they exhibited specific capacitance values of 8 and 90 F g^{-1}, respectively (Fig. 4a and Table S5). CV of Cu-CP@GO deviated from the rectangular shape characteristics of electrical double layer capacitors (EDLCs), and showed redox peaks, which correspond to both faradaic and non-faradaic charge storage mechanism processes. The plausible mechanism for the redox activity of Cu-CP@GO is illustrated in Scheme 2. In the composite, Cu(II) metal centers combined the benefits of redox-active ligands based on naphthalene diimide (NDI) of the DPNDI linker, which undergoes two successive one-electron redox processes that arise from reduction of NDI core motifs of Cu-CP to the radical anion $NDI^{\bullet -}$ and dianion NDI^{2-} species, respectively.[45] The broadening or suppression of the redox peaks in phosphate buffer was not due to loss of redox

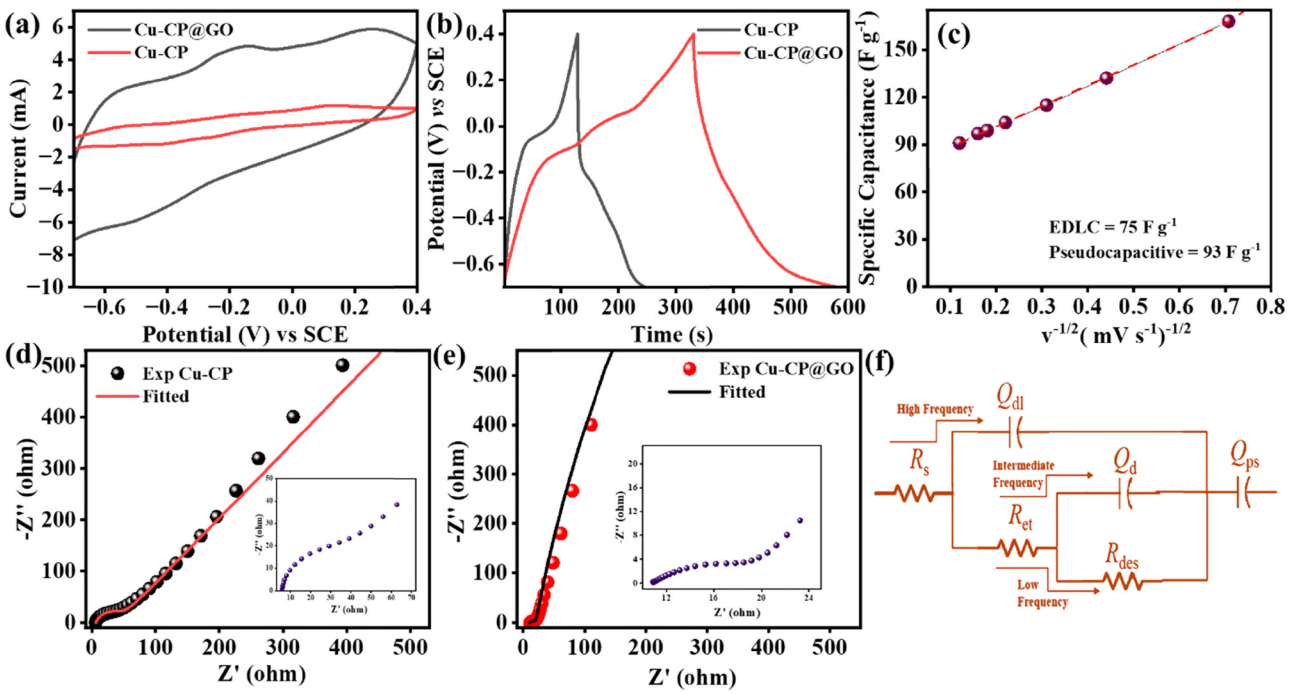

Fig. 4 Comparison of the curves of Cu-CP and Cu-CP@GO. (a) CV curves at 50 mV s^{-1} and (b) GCD curves at 0.6 A g^{-1}. (c) Plot of specific capacitance *vs.* the inverse of the square root of the scan rate showing the contribution of pseudocapacitance and EDLC for Cu-CP@GO. Comparison of the Nyquist plot of (d) Cu-CP and (e) Cu-CP@GO, and (f) equivalent circuit model for fitting of the Nyquist plot of Cu-CP and Cu-CP@GO.

reactivity, but rather due to electrolyte-mediated kinetic and interfacial suppression.[55]

The highest specific capacitance values obtained for Cu-CP and Cu-CP@GO were 96 and 168 F g^{-1} at scan rates of 2 mV s^{-1}, respectively (Table S5). The higher capacitance of the Cu-CP@GO material can be attributed to the incorporation of GO into Cu-CP, as GO contributes to electric double-layer capacitance and pseudocapacitance, resulting in boosted conductivity of the composite material.[56] As the scan rate was increased from 2 to 50 mV s^{-1}, the CV curves of both materials showed higher CV area under the curves without deformation and an increased current response, demonstrating good charge storage properties even at higher rates (Fig. S11). Additionally, Cu-CP@GO exhibited good capacitive retention at higher scan rates, maintaining 54% of its initial capacitance (Fig. S12).

The supercapacitor properties of both materials were further evaluated by galvanostatic charge–discharge (GCD) experiments. The GCD curves at a current density of 0.6 A g^{-1} within the potential interval −0.7 to 0.4 V *vs.* SCE demonstrate that Cu-CP@GO had a high charge–discharge time over Cu-CP, indicating its improved specific capacitance (Fig. 4b). The capacitance value obtained from GCD matched with the capacitance obtained from CVs. The behavior of the GCD curves was not linear, indicating that the charge storage mechanism involved both EDLC and faradaic redox reactions. The highest specific capacitance value obtained from GCD is 67 and 178 F g^{-1} at 0.6 A g^{-1} for Cu-CP and Cu-CP@GO, respectively. The GCD curves of both materials were recorded at different current densities ranging from 0.6 to 10 A g^{-1} (Fig. S13 and Table S6), demonstrating that discharge time decreased with increasing current density. At high current density, the charge/discharge process occurred rapidly only at surface or near-surface redox sites, which decreased the rate of ionic diffusion and electron transport, resulting in a decrease in specific capacitance.[57] Additionally, Cu-CP@GO exhibited good capacitive retention, maintaining ∼40% of its initial capacitance up to a current density of 10 A g^{-1} (Fig. S14). Cu-CP@GO exhibited enhanced electrical conductivity (*vide supra*), which led to a superior charge storage efficiency of Cu-CP@GO compared to Cu-CP. The contribution of the EDLC and faradaic processes to the capacitance of Cu-CP@GO can be expressed as the sum of a rate-independent parameter (k_1) for EDLC and a diffusion-controlled component (k_2), which is proportional to the square root of the inverse of the scan rate, as shown below in eqn (1).[32,58]

$$c = k_1 + k_2 v^{-1/2} \quad (1)$$

Following this equation, the intercept of the plot (c *vs.* $v^{-1/2}$) provides the EDLC contribution (k_1). For the Cu-CP@GO composite, a higher capacitance value of 93 F g^{-1} was associated with pseudocapacitive behavior from the redox-active linker and the oxygen functionalities of GO. Meanwhile, the EDLC contribution of 75 F g^{-1} was due to the high electrical conductivity offered by GO. Hence, the Cu-CP@GO composite exhibited better capacitive performance compared to Cu-CP, with GO enhancing both pseudocapacitance and EDLC. The Nyquist plots derived from EIS analysis exhibited a nearly vertical rise along the imaginary axis with a slight inclination towards the real axis of impedance for Cu-CP@GO in comparison to Cu-CP, indicating superior capacitive performance for Cu-CP@GO compared to Cu-CP (Fig. 4d and e). The Bode plots from EIS analysis indicated phase angles of 52° for Cu-CP and 74° for Cu-CP@GO in the low-frequency region (Fig. S15 and Table S7), approaching the ideal capacitive response of 90°, thereby confirming the outstanding supercapacitor performance of Cu-CP@GO.

Since Cu-CP@GO exhibited improved performance in a three-electrode system, the material was also investigated in a two-electrode cell for real-time applications, wherein a solid-state symmetric supercapacitor device with both platinum-coated positive and negative electrodes was employed.

It is well-known that the presence of pyridinic-N moieties is a basic feature of the carbon interface since they donate electrons. This makes acid electrolyte H_2SO_4 more appropriate for achieving additional double-layer capacitance than the other electrolytes.[59] Besides, the use of liquid electrolytes in supercapacitors is limited due to the risk of leakage and their susceptibility to evaporation. Gel polymer electrolytes (GPEs) resolve the leakage issue by immobilizing liquid electrolytes in a polymer matrix.[60] Additionally, GPEs can inhibit water oxidation reactions since they contain less free water than the liquid electrolytes, which have long been a problem with aqueous electrolyte-based supercapacitors. Consequently, the liquid electrolyte H_2SO_4 embedded in a matrix of PVA (PVA/H_2SO_4) has been used as an electrolyte for two-electrode studies. PVA has –OH groups that allow it to store water and promote efficient ion-conducting pathways. A Swagelok cell was used to assemble all the components, with a Whatman paper immersed in PVA/H_2SO_4 serving as an electrolyte and a separator. The CV and GCD studies of the two-electrode device were carried out in a potential window of 0.9 V (−0.5 to 0.4 V). CV curves illustrate a nearly rectangular shape and a negligible distortion even at high scan rates, indicating high supercapacitive behavior (Fig. 5a). Redox humps in CV around −0.11 and −0.24 V were observed owing to the pseudocapacitive contribution of oxygen functionalities of GO, which further contributed toward specific capacitance.[61] Cu-CP@GO exhibited a maximum specific capacitance of 118 F g^{-1} at a scan rate of 2 mV s^{-1} (Table S8). Furthermore, the GCD revealed nearly triangular curves that exhibited the maximum specific capacitance of 93 F g^{-1} at a current density of 0.5 A g^{-1} (Fig. 5b and Table S9) and retained nearly 56% capacitance up to a scan rate of 50 mV s^{-1} (Fig. 5c). Cycling stability of the Cu-CP@GO composite was tested up to 5000 cycles at a high scan rate of 50 mV s^{-1}, which exhibited 96% retention of its initial capacitance (Fig. 5d). It was observed that there was a slight increase in stability up to 2000 cycles, which could be due to the enhanced wettability of the material with time.[62] PXRD patterns of Cu-CP@GO before and after cycling are shown in Fig. S16. After cycling, a slight change in the peak intensities and drifts was observed, which could be due to a phase change. TEM images

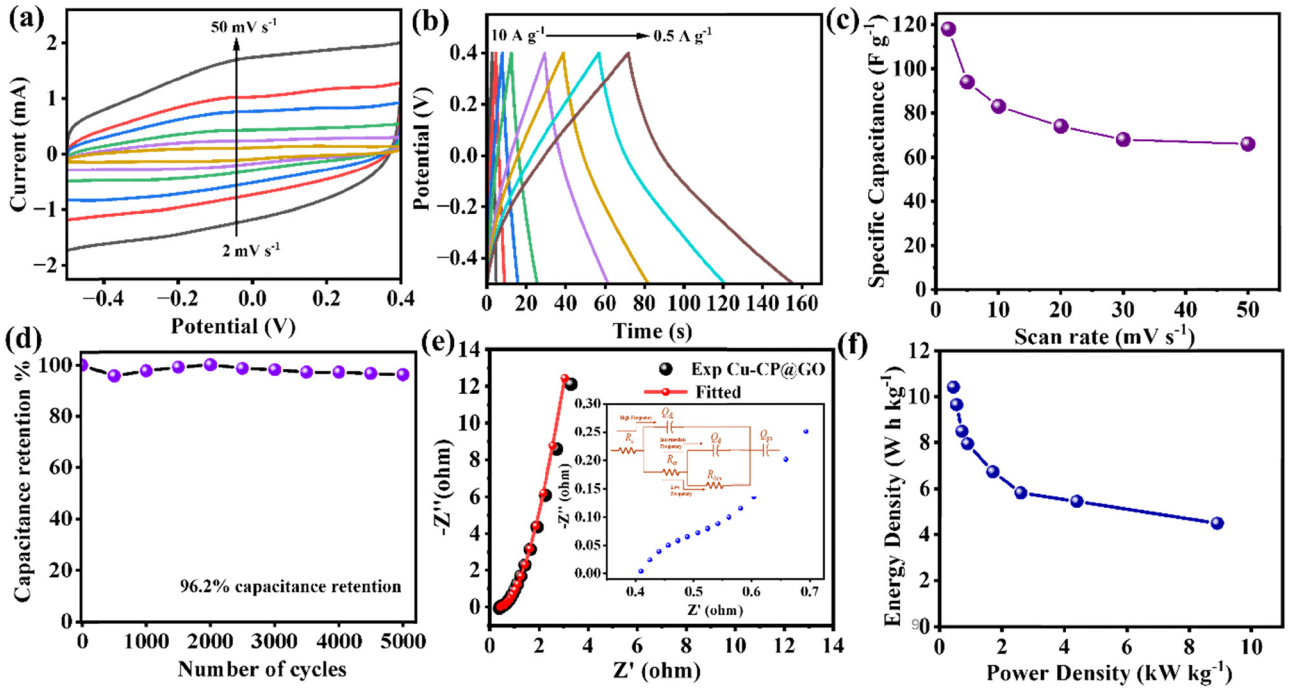

Fig. 5 Two-electrode device electrochemical studies of Cu-CP@GO. (a) CV curves at varied scan rates of 2–50 mV s^{-1}, (b) GCD curves at varied current densities of 0.5–10 A g^{-1}, (c) capacitance retention with the scan rate, and (d) cycling stability up to 5000 cycles at 50 mV s^{-1}. (e) Nyquist plot (inset: High frequency range and circuit) and (f) Ragone plot.

of Cu-CP@GO after the electrochemical cycling test showed no discernible morphological changes even after 5000 cycles, indicating structural stability throughout the cycling process (Fig. S17). The EIS analysis was carried out for a two-electrode symmetric device, with the results being represented through the Nyquist plot, demonstrating superior capacitive behavior, and the equivalent circuit is presented in the inset (Fig. 5e). The results from equivalent circuit parameters are listed in Table S10. The Bode plot from the EIS analysis exhibited a phase angle of 78.4°, further confirming the material's excellent supercapacitor performance (Fig. S18). According to the Ragone plot, Cu-CP@GO for a symmetric two-electrode device delivered a maximum energy density of 10.4 Wh kg^{-1} at a power density of 0.44 kW kg^{-1} (Fig. 5f). These values indicated a significant improvement in the energy density of Cu-CP@GO. Different supercapacitor parameters of Cu-CP@GO have been compared with those of previously reported similar state-of-the-art materials, as well as activated carbon materials in Tables S11 and S12. The comparison reveals that Cu-CP@GO is a potential material for energy storage, not only due to its notable capacitance values in a two-electrode symmetric device but also due to the material's exceptional cycling stability.

The stable electrochemical performance can be attributed to the high electrical conductivity of Cu-CP@GO due to π-conjugation and redox reactions of the DPNDI ligand of Cu-CP, as well as due to the presence of oxygen functionalities in the GO sheets, which contributed both EDLC and pseudocapacitance properties. Furthermore, graphite oxide (GO) can stabilize *in situ*-generated naphthalenediimide (NDI) radical anions through a combination of π–π stacking, hydrogen bonding, and electrostatic interactions.[62] Oxygen-containing functional groups and the GO structure presumably provided a platform for NDI moieties of Cu-CP to interact and provided stability for *in situ* generated radical anions, which contributed towards the long cycling stability of Cu-CP@GO. Indeed, it is delightful to note that radical anions were stable up to 5000 cycles, wherein the experiment was performed for 50 h.

Solid-state proton conductivity studies

The diverse functionalization of Cu-CP@GO encouraged us to estimate the applicability of the material as a solid-state proton conductor over a wide range of temperatures and humidities. Solid-state proton conductivity was studied by electrochemical impedance spectroscopy (EIS) using a compressed pellet. The resistance of proton transport within the solid pellet (R_{pc}) was determined from the diameter of a semicircular arc attained in the high-frequency region of the Nyquist plot, wherein the imaginary impedance (Z'') was plotted against the real impedance (Z'). Afterwards, the proton conductivities (σ_{pc}) were determined by using the dimensions of the pellet and the R_{pc} values, applying eqn (S7). The data obtained were fitted to an equivalent circuit model as shown in the inset of Fig. S19. EIS results revealed two semicircles wherein the first semicircle in the high frequency region corresponds to charge transfer resistance due to solid-state proton conduction, and the second semicircle in the low frequency region corresponds to resistance due to diffusion.[63] The capacitive components of the system are described using the constant phase elements

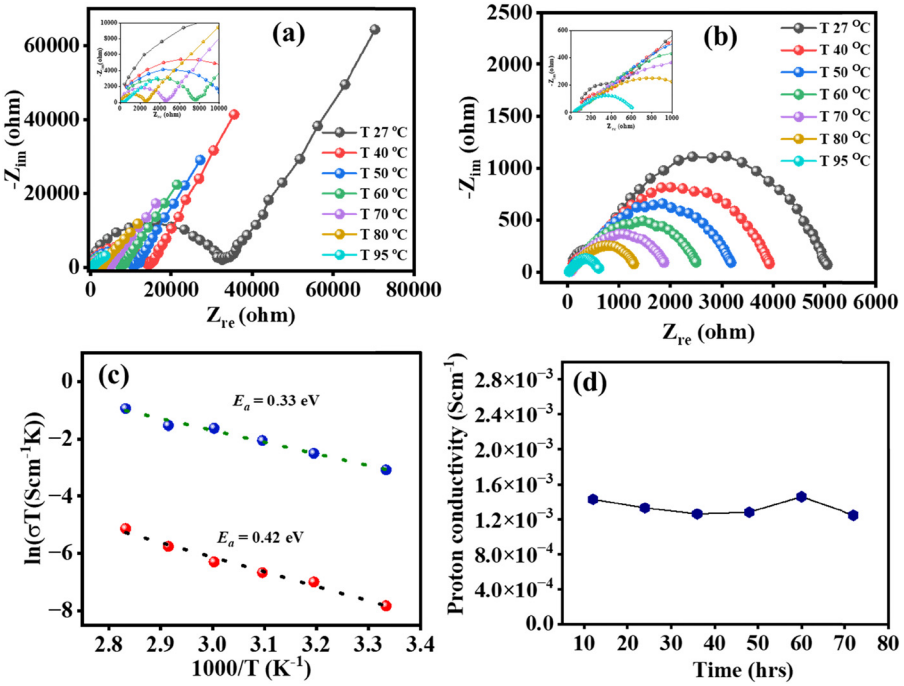

Fig. 6 (a) and (b) Nyquist plot of Cu-CP and Cu-CP@GO at 95% relative humidity. (c) Plot of ln(σT) at 95% RH for Cu-CP and Cu-CP@GO, wherein σ and T are proton conductivity and temperature. (d) Long term stability test for Cu-CP@GO at 95 °C and 95% RH.

(CPE-1 and -2) in response to the effects of system heterogeneity and surface roughness.[64]

At room temperature, Cu-CP displayed a proton conductivity of 1.5×10^{-6} S cm^{-1} under fully hydrated conditions (95% RH), which increased to 1.5×10^{-4} S cm^{-1} at 95 °C (Fig. 6a and Table S13). The low conductivity is attributed to the absence of less mobile protons within the framework. Interestingly, Cu-CP@GO displayed excellent proton conductivity of 1.5×10^{-4} S cm^{-1} at room temperature (95% RH), which increased to 1.4×10^{-3} S cm^{-1} at 95 °C, 95% RH (Fig. 6b and Table S14). Furthermore, it showed weak humidity dependence at room temperature with proton conductivity increasing from 1.2×10^{-4} S cm^{-1} at 40% RH to 1.5×10^{-4} S cm^{-1} at 95% RH (Fig. S19 and Table S15). GO introduced additional hydrophilic functionalities in the composite, which facilitated hydrogen bonding with water molecules and enhanced proton conductivity.[30] To gain further insights into the proton transfer mechanism, activation energy was determined from the Arrhenius plot. Fig. 6c shows activation energy (E_a) for both materials, which was found to be 0.42 eV for Cu-CP while 0.33 eV for Cu-CP@GO, suggesting vehicular and Grotthuss mechanisms of proton transport, respectively.[65] Furthermore, a long-term stability test was performed for Cu-CP@GO, wherein no decline in performance was observed for 72 h (Fig. 6d). This suggests that the material can be utilized for real-time applications.

Conclusion

In summary, a redox-active Cu-CP has been synthesized under ambient conditions and further grown on graphite oxide (GO) using a solvothermal approach to prepare a Cu-CP@GO composite. In terms of the electrochemical properties, Cu-CP containing a redox-active core offered enhanced and promising redox characteristics, while GO offered electrical conductivity along with rapid charge transportation, leading to remarkable electrochemical performance of Cu-CP@GO for supercapacitor and proton conduction applications. Cu-CP@GO exhibited a high specific capacitance of 178 F g^{-1} at 0.6 A g^{-1}, 1.8 times higher than that of pristine Cu-CP, in a three-electrode configuration. Additionally, an assembled two-electrode symmetric device of Cu-CP@GO exhibited excellent specific capacitance of 93 F g^{-1} at 0.5 A g^{-1} with excellent cycling stability of 96% after 5000 cycles. The improved supercapacitor performance of Cu-CP@GO was attributed to the enhanced electrical conductivity (1.14×10^{-1} S cm^{-1} for Cu-CP@GO and 8.1×10^{-2} S cm^{-1} for Cu-CP) offered by the synergistic effect of both CP and GO, which improved charge transfer at the electrode–electrolyte interface. It is important to note that Cu-CP@GO maintained 96% cycling stability after 5000 cycles, *i.e.* 50 h in a two-electrode configuration, in spite of *in situ* generation of radical anions during redox reactions. This was presumably due to excellent charge delocalization in GO and the NDI's π network. Additionally, Cu-CP@GO demonstrated a superior proton conductivity of 1.4×10^{-3} S cm^{-1} at 95 °C and 95% RH with a low activation barrier compared to Cu-CP. This could be due to the incorporation of GO, which introduced additional hydrophilic functionalities in the Cu-CP@GO composite to facilitate hydrogen bonding with water molecules. Finally, it is worth mentioning that the surface area and pore volume of these materials were low, and in spite of this challenge, Cu-CP@GO exhibited exceptional supercapacitor and solid-state proton conduction

performances. With strategies that involve enhancing the surface area, these materials can demonstrate exceptional performance in energy research.

Conflicts of interest

The authors declare no conflict of interest.

Data availability

All data generated and analyzed during this study have been included in the main manuscript and supplementary information (SI). Supplementary information: graphs and tables. See DOI: **https://doi.org/10.1039/d5nj03093e**.

CCDC 2476844 contains the supplementary crystallographic data for this paper.[66]

Acknowledgements

We acknowledge IISER Bhopal for infrastructural and financial support. R.R acknowledges Anusandhan National Research Foundation (ANRF), New Delhi for the National Postdoctoral Fellowship (PDF/2023/000025). We acknowledge FIST-supported TEM facility to the Department of Chemistry, IISER Bhopal. S. G. acknowledges IISER Bhopal for the PhD fellowship. We sincerely thank Dr Ravi Shankar Singh and Deepali Sharma, Department of Physics, IISER Bhopal for the support in conducting and analyzing the XPS results.

References

1 Y. Wang, Y. Song and Y. Xia, *Chem. Soc. Rev.*, 2016, **45**, 5925–5950.
2 M. Winter and R. J. Brodd, *Chem. Rev.*, 2004, **104**, 4245–4270.
3 M. Mastragostino, F. Soavi and C. Arbizzani, in *Advances in Lithium-Ion Batteries*, ed. W. A. Van Schalkwijk and B. Scrosati, Springer US, Boston, MA, 2002, pp. 481–505.
4 (*a*) M. Zhu, Y. Yang and Y. Ma, *Green Chem.*, 2023, **25**, 10263–10303; (*b*) Y. Yang, Y. Ma, C. Lu, S. Li and M. Zhu, *Green Chem.*, 2023, **25**, 10209; (*c*) R. T. Yadlapalli, R. R. Alla, R. Kandipati and A. Kotapati, *J. Energy Storage*, 2022, **49**, 104194.
5 B. Daffos, P.-L. Taberna, Y. Gogotsi and P. Simon, *Fuel Cells*, 2010, **10**, 819–824.
6 E. Raymundo-Piñero, K. Kierzek, J. Machnikowski and F. Béguin, *Carbon*, 2006, **44**, 2498–2507.
7 F. Stoeckli and T. A. Centeno, *J. Mater. Chem. A*, 2013, **1**, 6865–6873.
8 M. Islam, Md. S. Hossain, B. Adak, M. M. Rahman, K. K. Moni, A. S. M. Nur, H. Hong, H. Younes and S. Mukhopadhyay, *J. Energy Storage*, 2025, **107**, 114838.
9 F. Stoeckli and T. A. Centeno, *J. Mater. Chem. A*, 2013, **1**, 6865.
10 S.-J. Shin, J. W. Gittins, C. J. Balhatchet, A. Walsh and A. C. Forse, *Adv. Funct. Mater.*, 2024, **34**, 2308497.
11 M. Wang, R. Dong and X. Feng, *Chem. Soc. Rev.*, 2021, **50**, 2764–2793.
12 R. Rajak, R. Kumar, S. N. Ansari, M. Saraf and S. M. Mobin, *Dalton Trans.*, 2020, **49**, 11792–11818.
13 V. F. Yusuf, N. I. Malek and S. K. Kailasa, *ACS Omega*, 2022, **7**, 44507–44531.
14 E. R. Engel and J. L. Scott, *Green Chem.*, 2020, **22**, 3693–3715.
15 T. Yamada, K. Otsubo, R. Makiura and H. Kitagawa, *Chem. Soc. Rev.*, 2013, **42**, 6655–6669.
16 X. Huang, S. Zhang, L. Liu, L. Yu, G. Chen, W. Xu and D. Zhu, *Angew. Chem.*, 2018, **130**, 152–156.
17 R. Rajak, M. Saraf, A. Mohammad and S. M. Mobin, *J. Mater. Chem. A*, 2017, **5**, 17998–18011.
18 R. Rajak, M. Saraf, S. K. Verma, R. Kumar and S. M. Mobin, *Inorg. Chem.*, 2019, **58**, 16065–16074.
19 K. Wang, Y. Li, L.-H. Xie, X. Li and J.-R. Li, *Chem. Soc. Rev.*, 2022, **51**, 6417–6441.
20 M. Ko, L. Mendecki and K. A. Mirica, *Chem. Commun.*, 2018, **54**, 7873–7891.
21 H. Zhong, M. Wang, G. Chen, R. Dong and X. Feng, *ACS Nano*, 2022, **16**, 1759–1780.
22 F. Ahmed, B. Dutta and M. Hedayetullah Mir, *Dalton Trans.*, 2021, **50**, 29–38.
23 H. Zhang, Y. Zhang, C. Gu and Y. Ma, *Adv. Energy Mater.*, 2015, **5**, 1402175.
24 J. Calbo, M. J. Golomb and A. Walsh, *J. Mater. Chem. A*, 2019, **7**, 16571–16597.
25 Y. Zhou and L. Han, *Coord. Chem. Rev.*, 2021, **430**, 213665.
26 Y.-L. Mao, J. Yu, B.-Y. Shan, X.-X. Liu, J.-Y. Chu, X.-Y. Ma, M. Li, Y.-M. Zheng, B.-L. Zhu, M.-H. Zuo and S.-X. Cui, *New J. Chem.*, 2025, **49**, 7126–7133.
27 B. Tian, G.-H. Ning, Q. Gao, L.-M. Tan, W. Tang, Z. Chen, C. Su and K. P. Loh, *ACS Appl. Mater. Interfaces*, 2016, **8**, 31067–31075.
28 M. Shaheen, M. Z. Iqbal, M. W. Khan, S. Siddique, S. Aftab and S. M. Wabaidur, *Energy Fuels*, 2023, **37**, 4000–4009.
29 D. R. Chowdhury, C. Singh and A. Paul, *RSC Adv.*, 2014, **4**, 15138–15145.
30 S. Gupta and A. Paul, *Chem. Commun.*, 2025, **61**, 7604–7607.
31 A. K. Geim and K. S. Novoselov, *Nat. Mater.*, 2007, **6**, 183–191.
32 A. Barua, P. Mehra and A. Paul, *ACS Appl. Energy Mater.*, 2021, **4**, 14249–14259.
33 R. Rajak, M. Saraf and S. M. Mobin, *J. Mater. Chem. A*, 2019, **7**, 1725–1736.
34 S. Gautam, S. Rialach, S. Paul and N. Goyal, *RSC Adv.*, 2024, **14**, 14311–14339.
35 G. Yang, D. Zhang, G. Zhu, T. Zhou, M. Song, L. Qu, K. Xiong and H. Li, *RSC Adv.*, 2020, **10**, 8540–8547.
36 Y.-R. Liu, Y.-Y. Chen, Q. Zhuang and G. Li, *Coord. Chem. Rev.*, 2022, **471**, 214740.
37 Afzal, Y. Ren, S. Wang, H. Ma, S. Yuan, Q. Zhao, M. B. Wadud, X. Liang, Q. Pan, G. He and Z. Jiang, *J. Membr. Sci.*, 2025, **722**, 123863.
38 D.-W. Lim and H. Kitagawa, *Chem. Soc. Rev.*, 2021, **50**, 6349–6368.

39 D.-W. Lim and H. Kitagawa, *Chem. Rev.*, 2020, **120**, 8416–8467.
40 Y.-S. Wei, X.-P. Hu, Z. Han, X.-Y. Dong, S.-Q. Zang and T. C. W. Mak, *J. Am. Chem. Soc.*, 2017, **139**, 3505–3512.
41 Q. Wu, Q. Li, W. Zou, Z. Zhang, Y. Zhou and Q. Zhao, *Chem. Commun.*, 2025, **61**, 1842–1845.
42 D. Jędrzejowski, M. Pander, E. Stachura, K. Matlak, W. Bury and D. Matoga, *J. Mater. Chem. A*, 2025, **13**, 23671–23679.
43 P. M. Unnikrishnan, G. Premanand and S. K. Das, *Inorg. Chem.*, 2025, **64**, 3506–3517.
44 C. Petit and T. J. Bandosz, *Adv. Mater.*, 2009, **21**, 4753–4757.
45 F. de A. Silva, G. Lima and G. J.-F. Demets, *Russ. J. Electrochem.*, 2022, **58**, 433–443.
46 B. Ding, B. Chan, N. Proschogo, M. B. Solomon, C. J. Kepert and D. M. D'Alessandro, *Chem. Sci.*, 2021, **12**, 3608–3614.
47 R. Rajak, M. Saraf and S. M. Mobin, *Inorg. Chem.*, 2020, **59**, 1642–1652.
48 P. Mehra, M. Wilson and A. Paul, *J. Phys. Chem. C*, 2022, **126**, 10534–10545.
49 C. Singh, S. Nikhil, A. Jana, A. K. Mishra and A. Paul, *Chem. Commun.*, 2016, **52**, 12661–12664.
50 S. H. Huh, H.-M. Ju and S.-H. Choi, *J. Korean Phys. Soc.*, 2010, **57**, 1649–1652.
51 M. Thommes, K. Kaneko, A. V. Neimark, J. P. Olivier, F. Rodriguez-Reinoso, J. Rouquerol and K. S. W. Sing, *Pure Appl. Chem.*, 2015, **87**, 1051–1069.
52 R. Rajak, M. Saraf, P. Kumar, K. Natarajan and S. M. Mobin, *Inorg. Chem.*, 2021, **60**, 16986–16995.
53 H. Peng, Z. Mo, S. Liao, H. Liang, L. Yang, F. Luo, H. Song, Y. Zhong and B. Zhang, *Sci. Rep.*, 2013, **3**, 1765.
54 M. D. Makhafola, K. D. Modibane, K. E. Ramohlola, T. C. Maponya, M. J. Hato, K. Makgopa and E. I. Iwuoha, *Sci. Rep.*, 2021, **11**, 17219.
55 R. Gisbert, G. García and Marc T. M. Koper, *Electrochim. Acta*, 2010, **55**, 7961–7968.
56 S. Gautam, S. Rialach, S. Paul and N. Goyal, *RSC Adv.*, 2024, **14**, 14311–14339.
57 A. Mallick, H. Liang, O. Shekhah, J. Jia, G. Mouchaham, A. Shkurenko, Y. Belmabkhout, H. N. Alshareef and M. Eddaoudi, *Chem. Commun.*, 2020, **56**, 1883–1886.
58 T. Lin, I.-W. Chen, F. Liu, C. Yang, H. Bi, F. Xu and F. Huang, *Science*, 2015, **350**, 1508–1513.
59 M. Seredych, D. Hulicova-Jurcakova, G. Qing Lu and T. J. Bandosz, *Carbon*, 2008, **46**, 1475–1488.
60 S. Alipoori, S. Mazinani, S. Hamed Aboutalebi and F. Sharif, *J. Energy Storage*, 2020, **27**, 101072.
61 P. Simon, Y. Gogotsi and B. Dunn, *Science*, 2014, **343**, 1210–1211.
62 (*a*) A. Barua and A. Paul, *Energy Fuels*, 2021, **35**, 10262–10273; (*b*) B. Tang, J. Zhao, J.-F. Xu and X. Zhang, *Chem. Sci.*, 2020, **11**, 1192–1204; (*c*) S. V. Bhosale, M. A. Kobaisi, R. W. Jadhav, P. P. Morajkar, L. A. Jones and S. George, *Chem. Soc. Rev.*, 2021, **50**, 9845–9998.
63 H. L. Tuller, *Solid State Ionics*, 2000, **131**, 143–157.
64 C. Klumpen, S. Winterstein, G. Papastavrou and J. Senker, *J. Mater. Chem. A*, 2018, **6**, 21542–21549.
65 W. Münch, K.-D. Kreuer, W. Silvestri, J. Maier and G. Seifert, *Solid State Ionics*, 2001, **145**, 437–443.
66 CCDC 2476844: Experimental Crystal Structure Determination, 2025, DOI: **10.5517/ccdc.csd.cc2p4c6f**.

